Contrib Mineral Petrol (1998) 133: 12–29

**Vratislav Hurai · Klaus Simon · Uwe Wiechert
Jochen Hoefs · Patrik Konečný · Monika Huraiová
Jacques Pironon · Jozef Lipka**

Immiscible separation of metalliferous Fe/Ti-oxide melts from fractionating alkali basalt: *P-T-f*$_{O_2}$ conditions and two-liquid elemental partitioning

Received: 30 September 1997 / Accepted: 23 March 1998

Abstract Globules of iron-dominated (59–69 wt% FeO_{tot}) and titanium-dominated (43.5 wt% TiO_2) oxide melts have been detected in igneous xenoliths from Pliocene-to-Pleistocene alkali basalts of the Western Carpathians. Fluid inclusion and mineral composition data indicate immiscible separation of the high-iron-oxide melt (HIM) at magmatic temperatures. The HIM separation occurred during clinopyroxene (augite) accumulation in an alkali trachybasalt and continued during crystallization of amphibole (kaersutite) and K-feldspar (anorthoclase), the latter coexisting with trachyte and alkalic rhyolite residual melts. Some HIM was also expelled from sub-alkalic rhyolite (70–77% SiO_2), coexisting with $An_{27–45}$ plagioclase and quartz in granitic (tonalite-trondhjemite) xenoliths. Oxygen fugacities during HIM separation range from −1.4 to +0.6 log units around the QFM buffer. A close genetic relationship between HIM-hosted xenoliths and mantle-derived basaltic magma is documented by mineral $\delta^{18}O$ values ranging from 4.9 to 5.9‰ V-SMOW. δD values of gabbroic kaersutite between −61 and −86‰ V-SMOW are in agreement with a presumed primary magmatic water source. Most trace elements, except Li, Rb and Cs, have preferentially partitioned into the HIM. The HIM/Si-melt partition coefficients for transition elements (Sc, V, Cr, Co, Ni) and base metals (Zn, Cu, Mo) are between 2–160, resulting in extreme enrichment in the HIM. La and Ce also concentrate in the silicic melt, whereas Tb-Tm in the HIM. Hence, the immiscible separation causes REE fractionation and produces residual silicic melt enriched in LREE and depleted in HREE. The weak fractionation among Tb-Tm and Yb, Lu can be attributed to recurrent extraction of the HIM from the magmatic system, while flat HREE chondrite-normalized patterns are interpreted to indicate no or little loss of the HIM.

V. Hurai · P. Konečný
Geological Survey, Mlynská dolina 1, 817 04 Bratislava, Slovak Republic

K. Simon · U. Wiechert · J. Hoefs
Geochemisches Institut der Universität, Goldschmidtstr. 1, D-37077 Göttingen, FRG

M. Huraiová
Dept. of Mineralogy and Petrology, Comenius University, 841 05 Bratislava, Slovak Republic

J. Pironon
CREGU-CNRS, BP 23, F-54501 Vandœuvre-lès-Nancy, France

J. Lipka
Dept. of Nuclear Physics and Technology, Slovak Technical University, 812 19 Bratislava, Slovak Republic

Editorial responsibility: T. L. Grove

Introduction

Since the discovery by Roedder and Weiblen (1971) of immiscible silicate melts in lunar and terrestrial basalts, a relatively large number of studies have postulated a significant role for immiscibility in the petrogenesis of igneous rocks. In terrestrial samples, conjugate melts have been observed in quenched residual liquid (mesostasis) between plagioclase and pyroxene crystals in tholeiitic and alkali basalts (Roedder and Weiblen 1971; Roedder 1979; Philpotts 1982), and less frequently in melt inclusions trapped in olivine (Roedder and Weiblen 1971). Most of the published works address the immiscibility between melts of ferropyroxenite composition (25–40% FeO_{tot}, 35–45% SiO_2) and plagiogranite, typically containing 71–79 wt% SiO_2 (Roedder 1979; Philpotts 1982; Philpotts and Doyle 1983).

Although there is abundant field evidence for an iron oxide-dominated magma (e.g., Park 1961; Frietsch 1978; Nystrøm and Henriquez 1994; Förster and Jafarzadeh 1994), direct observations for coexisting immiscible silicate and iron-oxide glasses are lacking. Iron ± titanium ± phosphorus melts have been produced experimentally by immiscible separation from the silica-rich liquids (e.g., Philpotts 1967; Naslund 1983). Naumov et al. (1993) described, in melt inclusions from quartz phenocrysts of ignimbrites, naturally occurring

iron-oxide globules of average composition (wt%): 81.2 ± 3.4 FeO, 2.2 ± 0.6 Al_2O_3 and 9.9 ± 1.2 SiO_2, coexisting with rhyolite glass (70.2 ± 1.0 SiO_2, 17.2 ± 0.5 Al_2O_3, 6.7 ± 0.9 K_2O, 3.7 ± 0.3 Na_2O, 0.32 ± 0.14 FeO) . Dissolution of the Fe-globules in the Si-rich melt took place at 1050–1100 °C. The FeO content of the bulk melt was recalculated to reach 0.98 wt%. Worthy of note was the paucity of TiO_2 (0–0.2 wt%), as well as ZnO content between 0.16 and 0.22% in the Fe-globules.

The objective of this paper is to describe a **high-iron-oxide melt (HIM)**, containing 59–69 wt% FeO_{tot} and 6–24 wt% SiO_2. In addition, a titanium oxide-dominated melt (43.5 wt% TiO_2) is reported from another locality. The Fe(Ti)-oxide melts were found in igneous xenoliths ejected during phreato-magmatic eruptions of alkali basalts. It will be argued that the HIM-bearing igneous xenoliths result from crystal fractionation in a deep-crustal chamber of alkali basalt magma, and that the HIM represents a primary magmatic phase.

Geological background and sample location

A relatively small volcanic field extends for some 20 km^2 in the northern part of the Pannonian basin, along the state boundary between Slovakia and Hungary (Fig. 1). Basaltic volcanism in this area is attributed to local Pliocene-Pleistocene extension superimposed on a subduction-related Miocene volcanic field of andesites and rhyolites. According to radiometric, biostratigraphic and paleogeographic data, a total of six phases of basaltic volcanism has been distinguished, spanning the time interval between Pontian (6.44 Ma) and Pleistocene (Konečný V. et al. 1995). Volcanism is believed to represent a link with lithosphere thinning and partial melting induced by local mantle upwelling (Konečný P. et al. 1995).

Igneous xenoliths of exotic composition were first described by Huraiová et al. (1996) from a Pliocene (Pontian) maar structure near Pinciná formed during the first volcanic phase. More detailed inspection has confirmed the occurrence of xenoliths in various volcanic products (diatremes, maars, lava flows) throughout the territory. A tuff cone near Hodejov, created during the latest (Pleistocene) volcanic phase, is the additional locality studied. Both structures are situated at the northern periphery of the volcanic field, some 17 km apart (Fig. 1).

Angular-to-rounded xenoliths occur within basaltic bombs, or as single fragments embedded in lapilli tuffs ranging from several cm to as much as 0.5 m in size. Igneous xenoliths, low-grade metamorphic rocks, quartz

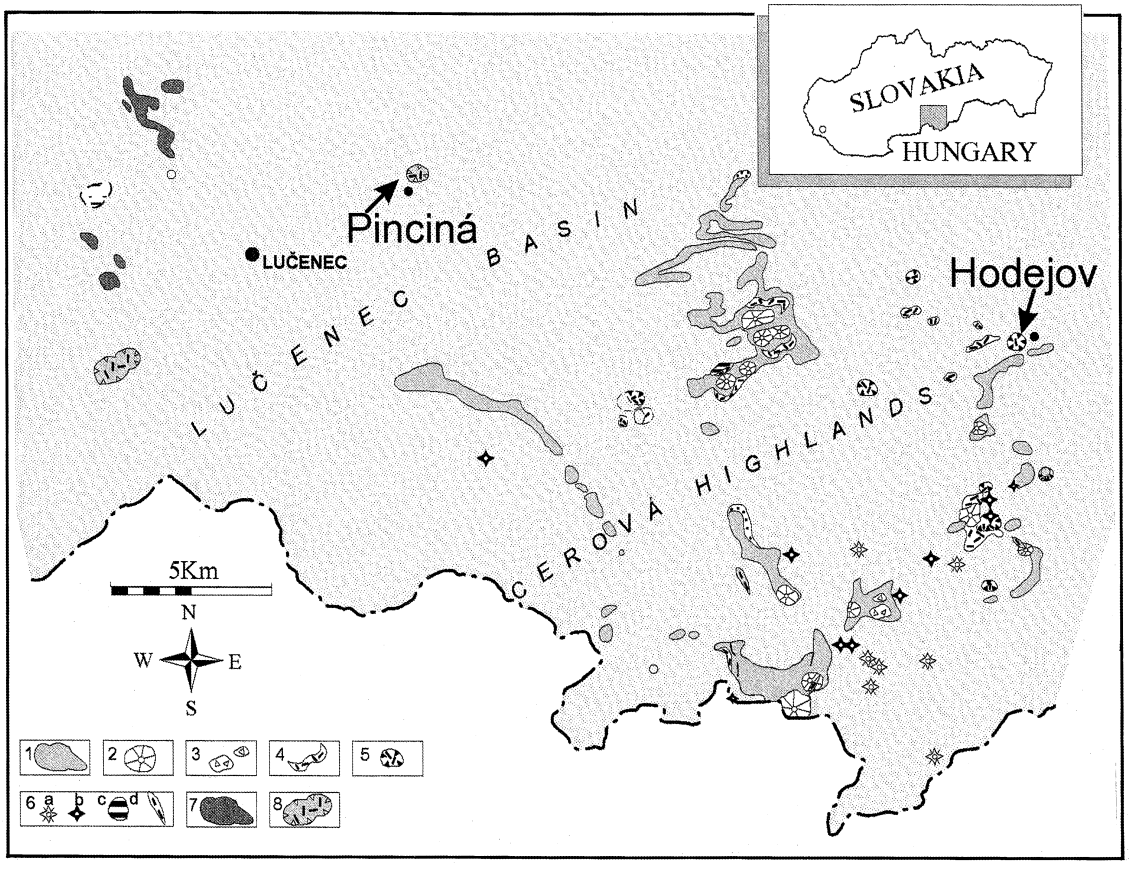

Fig. 1 Basaltic volcanic field in southern Slovakia. The Cerová formation (Pliocene-Pleistocene): *1* lava flow, *2* scoria cone, *3* agglomerate, *4* lapilli tuff, *5* maar, *6* eruptive centres: *a* diatreme, *b* neck, *c* extrusion, *d* dyke. The Podrečany formation (early Pliocene): *7* lava flow, *8* maar

vein fragments and Miocene sediments have been encountered in explosive basalts. In contrast, superimposed effusive basaltic lava flows contain predominantly Cr-diopside-bearing upper mantle xenoliths, with spinel lherzolite and harzburgite as the most abundant rock species (Konečný P. et al. 1995).

The igneous xenoliths can be divided into mafic and felsic types. The mafic (gabbroic) xenoliths are clinopyroxene-plagioclase and amphibole-plagioclase cumulates. Clinopyroxene (TiAl-augite), amphibole (FeTi-pargasite, kaersutite), and calcic plagioclase ($An_{53–64}$) are the dominant mineral phases (Tables 1, 2). Olivine ($Fo_{73–75}$) and Fe, Mg, Al-spinel (pleonaste) are relatively abundant in the cpx-plg cumulates, whereas minor biotite and clinopyroxene are present in the am-plg xenoliths.

The felsic xenoliths can be subdivided into syenitic and granitic types. Syenite is composed of K-feldspar ($Ab_{60–83}$ $An_{2–11}$ $Or_{10–39}$), zircon and up to 15 vol.% of interstitial glass (Table 3). Accessory minerals include spinel, amphibole, corundum, apatite, sphene, monazite, xenotime and a plethora of Nb, Th, U, Y-oxides and complex Y,REE-bearing silicates. The granitic xenoliths correspond to tonalite or trondhjemite. They are composed of quartz, plagioclase ($Ab_{59–67}$ $An_{27–37}$ $Or_{4–8}$) and 40–50 vol.% of rhyolite glass, which may contain crystals of hypersthene and ilmenite (Table 4).

A total of seven HIM-containing xenoliths has been identified, of which the sample HO-1 is an amphibole-dominated cumulate from Hodejov and the remaining samples include one amphibole-plagioclase cumulate (HP-1), four syenitic xenoliths (PI-14, PI-12, KP-9, HP-3) and one granitic xenolith (KP-31), all collected from the tuff cone near Pinciná.

Description of HIM and accompanying phases

The most spectacular evidence for two-liquid immiscibility has been obtained from glass pockets hosted by

Table 1 Representative electron microprobe analyses of rock-forming minerals in cpx-plg xenolith PI-13

Anal. No.	Ol #21	Cpx #46	Sp #88	Am #7	Plg #74
SiO_2	37.80	49.82	–	38.52	55.46
TiO_2	0.04	1.56	0.86	5.01	–
Al_2O_3	0.01	6.90	54.45	14.67	28.96
FeO	23.93	7.09	17.95	4.80	0.00
Fe_2O_3[a]	–	–	12.23	7.28	–
MnO	0.40	0.20	0.22	0.25	0.02
MgO	37.65	14.81	14.63	12.42	0.03
CaO	0.15	18.68	0.02	10.99	10.54
Na_2O	–	0.68	–	2.82	4.80
K_2O	–	0.02	–	0.72	0.25
Cr_2O_3	0.00	0.07	0.03	0.00	–
Total	99.98	99.81	100.39	97.48	100.06

[a] Recalculated from stoichiometry, total Fe as FeO in other analyses

Table 2 Average (∅) and representative (#) electron microprobe analyses of melts and minerals in am-plg gabbroic xenoliths

Sample	HP-1									HO-1	
Host	Plg	Am	Cpx	Cpx-hosted melt inclusion				Cpx	Am	Am	Am
Phase				Glass	Am	Sp	Bulk[a]	HIM	HIM		HIM
Anal. No.	#43	#62	#52	#54	#54b	#54a		#60	#67	#4	∅2
SiO_2	56.68	40.62	52.28	64.91	41.38	–	47.55	5.94	5.72	40.90	24.03
TiO_2	–	4.88	0.79	0.23	4.23	12.54	3.25	0.07	0.18	4.10	43.49
Al_2O_3	26.83	13.54	5.26	22.35	13.36	6.79	16.18	0.15	0.27	15.13	5.16
Fe_2O_3[b]	–	5.09	–	–	0.82	51.28	3.06	–	–	4.05	–
FeO	0.18	7.15	7.45	0.00	12.04	25.48	8.50	66.69	69.07	3.04	10.59
MnO	–	0.24	0.27	0.09	0.16	0.51	0.15	2.29	0.32	0.15	0.05
MgO	–	11.94	12.97	0.00	11.26	4.21	6.97	1.03	0.15	14.38	0.19
CaO	9.32	9.43	19.53	2.24	10.63	–	7.16	0.48	0.43	10.09	1.79
Na_2O	5.97	3.01	1.52	5.13	3.04	–	3.62	0.10	0.00	2.27	0.01
K_2O	0.43	0.70	0.00	3.29	0.88	–	1.68	0.03	0.07	1.58	0.22
Cr_2O_3	–	0.00	0.00	0.00	0.00	0.00	0.00	0.00	0.00	0.00	0.00
P_2O_5	–	–	–	0.79	0.06	–	0.31	0.10	0.25	–	1.43
Cl	–	0.00	–	0.17	0.02	–	0.07	0.04	0.12	0.00	0.00
Total	99.41	96.60	100.07	99.20	97.88	100.81	98.50	76.92	76.58	95.69	86.86

[a] Bulk melt recalculated from volumetric ratio of inclusion phases (glass 35, am 60, sp 5% – Fig. 4f)
[b] Fe_2O_3 recalculated from stoichiometry, total iron as FeO in remaining analyses

Table 3 Average (∅) and representative (#) electron microprobe analyses of melts and minerals in syenitic xenoliths

Sample	PI-12			KP-9						PI-14	
Host	Plg	Melt pocket		Plg	Plg	Melt pocket				Plg	Melt pocket
Phase		HIM	Glass		Glass	HIM	Glass	Usp	Ti, Si-Al		Glass
Anal. No.	#50	#37	∅14	#23	#22	∅2	∅3	#28	#28a	#41	∅4
SiO_2	66.33	8.04	62.91	67.26	68.88	10.43	65.65	2.06	22.67	67.03	63.54
TiO_2	–	0.00	0.09	–	0.00	0.23	0.00	16.19	36.40	–	0.12
Al_2O_3	20.02	0.06	19.57	20.80	17.76	0.60	19.56	10.43	21.30	19.85	19.76
FeO	0.00	68.24	3.06	0.00	0.00	63.26	1.86	29.22	3.09	0.00	2.01
Fe_2O_3[b]	–	–	0.67	–	–	–	1.12	38.36	–	–	1.42
MnO	0.03	1.94	0.37	–	0.09	1.99	0.13	0.80	0.24	–	0.32
MgO	0.00	0.27	0.44	–	0.00	0.48	0.29	1.64	0.06	–	0.30
CaO	1.22	0.18	0.74	1.69	0.53	0.45	0.78	0.13	0.99	0.76	1.00
Na_2O	8.25	0.00	5.14	9.71	5.16	0.07	6.12	–	0.03	8.20	5.67
K_2O	3.94	0.00	4.73	1.85	5.44	0.04	5.16	–	0.18	4.63	3.74
Cr_2O_3	–	0.00	0.00	–	0.00	0.00	0.00	0.00	0.00	–	0.00
P_2O_5	–	2.46	0.06	–	0.12	0.25	0.00	–	–	–	0.02
Cl	–	0.22	0.11	–	0.08	0.00	0.09	–	–	–	0.20
Total	99.79	81.41	97.88	101.31	98.06	77.80	100.77	98.83	84.96	100.46	98.09

Sample	HP-3						
Host	Plg	Zircon-hosted melt inclusions				Melt pocket	
Phase		Glass	Mag	Bulk[a]	Glass	Glass	HIM
Anal. No.	#36	#49	#52		#24	∅5	#22
SiO_2	67.35	61.94	0.23	57.62	66.33	64.10	10.98
TiO_2	–	0.11	0.46	0.13	0.00	0.12	0.04
ZrO_2	–	0.94	–	0.87	–	–	–
Al_2O_3	19.10	17.16	3.19	16.18	19.24	15.37	0.03
FeO	0.07	4.44	30.53	6.27	0.15	5.05	64.98
Fe_2O_3[b]	–	–	64.38	4.51	–	1.01	–
MnO	–	0.16	1.07	0.22	0.02	0.50	0.14
MgO	–	0.00	0.00	0.00	0.00	0.06	0.23
CaO	0.72	1.62	0.00	1.51	0.62	2.74	0.14
Na_2O	7.48	3.89	–	3.62	7.51	4.64	0.00
K_2O	5.77	4.32	–	4.02	5.57	4.47	0.00
Cr_2O_3	–	0.05	0.13	0.06	0.00	0.00	0.00
P_2O_5	–	0.04	–	0.04	0.02	0.07	0.43
Cl	–	0.30	–	0.28	0.00	0.02	0.00
Total	100.49	94.97	99.99	95.33	99.45	98.14	76.96

[a] bulk melt recalculated from volumetric ratio of inclusion phases (mag 7, glass 93% – Fig. 4b)
[b] Fe_2O_3 recalculated from stoichiometry (mag and usp), and estimated from ^{57}Fe Mössbauer spectroscopy (glass); total iron as FeO in remaining analyses

syenitic xenoliths. The pockets are rounded, isolated, 0.5–5 mm in diameter, interstitial to coarse grains of anorthoclase. Thin glassy veinlets have also been observed (Fig. 2a). The glass is transparent to translucent, strongly vesicular, in places slightly devitrified (Fig. 2c), often showing flow texture created by transparent yellow- and translucent-to-opaque brown-coloured domains. Boundaries between these domains are diffuse (Fig. 2b). The interstitial glass-hosted vesicles are either empty or filled with a low density vapour, as suggested by no phase transitions on freezing to −196 °C.

Reddish-brown HIM spherules occur in the brown domains of the glass pockets (Fig. 2b, c). Smaller HIM spherules, 2–5 μm in diameter, coalesce to form larger globules up to 50 μm in diameter, along grain-melt boundaries. Identical HIM globules were trapped as isolated inclusions, 50–200 μm, exceptionally 500–2000 μm in diameter, along growth planes within rock-forming plagioclase (Fig. 2e) and zircon (Fig. 2f, g). One HIM globule extracted from the plagioclase was 1 mm across. Scanning Electron Microscope (SEM) imagery of the polished HIM did not reveal any zoning or recrystallization. Centres of larger HIM globules are spongy, rims are compact.

Initially liquid state of the HIM globules is indicated by circular shapes (Fig. 2e–g), sharp curvilinear boundaries against silica-rich melt matrix (Fig. 2c, g), coarsening by coalescence along mineral surfaces and

Table 4 Representative electron microprobe analyses of melts and minerals in granitic xenolith KP-31

Host	Plg	Melt pocket				Opx
Phase		HIM	Glass	Opx	Ilm	Glass
Anal. No.	#120	#123	∅5	#118	#131	#125
SiO_2	61.90	23.85	72.38	52.50	0.02	74.97
TiO_2	–	0.37	0.87	0.12	51.23	0.87
Al_2O_3	24.18	1.94	12.49	0.55	0.14	11.44
FeO	0.00	58.10	2.38	29.54	42.20	2.75
Fe_2O_3[a]	–	–	0.29	–	2.07	–
MnO	–	0.14	0.14	1.13	0.77	0.15
MgO	–	0.32	0.63	15.65	2.87	0.13
CaO	6.02	1.06	1.60	1.56	0.05	1.58
Na_2O	7.63	0.25	2.71	0.29	–	2.29
K_2O	0.74	0.19	2.73	0.02	–	2.60
Cr_2O_3	–	0.00	0.00	0.00	0.00	0.00
P_2O_5	–	1.21	0.25	–	–	0.03
Cl	–	0.08	0.02	–	–	0.05
Total	100.47	87.51	96.49	101.36	99.35	96.86

[a] Recalculated from stoichiometry (ilm) and ^{57}Fe Mössbauer spectroscopy (glass), total Fe as FeO in remaining analyses

displacement along crosscutting cracks (Fig. 2e). Some HIMs are squeezed between plagioclase grains to acquire an elongate or deformed shape. Separate entrapment of Fe- and Si-rich conjugate phases in coeval primary inclusions unequivocally indicates a two-liquid immiscibility (Fig. 2h). The HIM spherules are sometimes accompanied by ulvöspinel, unidentified columnar, semi-transparent Ti-aluminosilicate crystals (Fig. 2d) and magnetite (Fig. 2h).

In the syenites KP-9 and PI-14, the HIM spherules have been encountered solely in centres of glass pockets, suggesting the onset of a two-liquid immiscibility subsequent to crystal growth. In contrast, the HIM spherules are dispersed within the glass pockets as well as rock-forming minerals in the samples HP-3 and PI-12, indicating the immiscible separation synchronous with the mineral crystallisation.

In granitic xenoliths, the rare HIM globules accompany ilmenite and hypersthene in interstitial rhyolitic melt. Most vesicles of the interstitial melt are empty, but many are filled with low salinity aqueous liquid. On freezing, some ''empty'' vesicles nucleate CO_2 solid at about −100 °C, which melts at −56.6 °C, creating a thin liquid rim coating the vesicle walls. Rock-forming minerals are devoid of the HIM, although silicate melt and CO_2 inclusions are frequent.

In gabbroic xenoliths, abundant HIM spherules are present along growth zones in kaersutite (Fig. 3), and also within clinopyroxene nucleation centres of larger kaersutite laths. The HIM occurs only in am-plg-dominated xenoliths. The associated cpx-plg cumulates contain only blebs of iron monosulfide melts. Interstitial silica-rich glasses are not present within the gabbroic xenoliths, however, silica-rich melt inclusions are frequent, particularly within clinopyroxene.

The HIMs are encapsulated in rock-forming minerals together with CO_2– and silica-rich melt inclusions (Fig. 4). The latter can be subdivided into:

(i) – *polyphase* (*crystallized*) *inclusions*, containing silica-rich glass, shrinkage bubble and daughter crystals represented by magnetite, hercynite, Ca, Y, REE-silicate, Y-silicate, U, Th-, U, Th, Y- and U, Th, Nb-oxides, phlogopite in syenitic xenoliths (Fig. 4a, b), and by kaersutite and spinel in gabbroic xenoliths (Fig. 4f),

(ii) – *two-phase inclusions* consisting of vapour bubble and a homogeneous silicate glass, devoid of daughter phases. The inclusions are characteristic of syenite plagioclase (Fig. 4e), but they have been rarely encountered also in zircon (Fig. 4c).

Carbon dioxide liquid occurs either within shrinkage bubbles of melt inclusions or in separate monophase inclusions in all types of xenoliths. Diameters of the primary inclusions are between 2–10 μm in syenite feldspar (Fig. 4d), 2–20 μm in a granite quartz, and 10–50 μm in clinopyroxene from gabbroic xenoliths. Many of the CO_2 inclusions are re-equilibrated, exhibiting planar fractures (plg, qtz) and/or wall recrystallization (cpx).

Analytical techniques

Major elements were measured with an electron microprobe at the Geological Survey of Slovakia in Bratislava. The microprobe used is a JEOL-733 SUPERPROBE with 15 kV accelerating voltage, beam integration, 10 s counting times, beam current 18–20 nA, specimen current of 16–18 nA on cup and spot size 10–15 μm^2 during glass and plagioclase analysis. Pure Si-, Ti-, Fe-, Al-, and Mg-oxides, wollastonite for Ca, rhodonite for Mn, chromite for Cr, albite for Na, orthoclase for K, halite for Cl and BaF_2 for F were used as standards. Analyses were corrected according to the ZAF scheme (Armstrong 1988).

Trace elements were analysed by inductively-coupled plasma mass spectrometry (ICP-MS) at the Institute of Geochemistry, Göttingen. 50 mg of plagioclase, 20 mg of silica-rich glass and 2–3 mg of HIM were hand-picked under a stereo-microscope. The HIM was separated from 1–2 kg of gently crushed plagioclase.

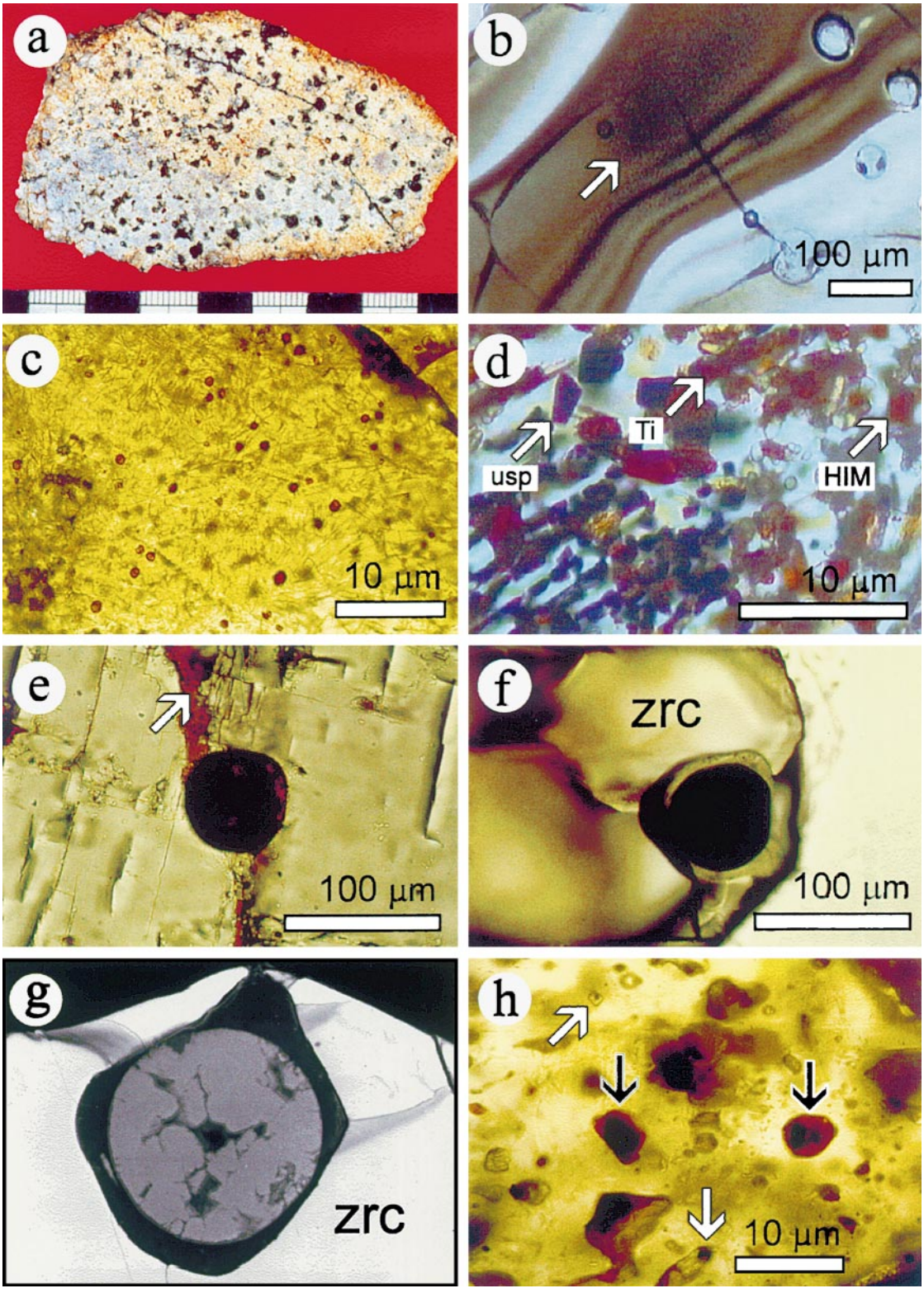

Fig. 2a–h High-iron oxide melt (HIM) and associated phases in syenitic xenoliths. **a** Thin veinlets and glass pockets as black spots in white anorthoclase. Sample HP-3, scale bar in cm. **b** Portion of a glass pocket with flow structure and several rounded vesicles in the right part. Tiny spherules of the HIM are clustered in the dark domains (*arrow*). Sample PI-14. **c** Glass pocket with small HIM spherules disseminated in partly devitrified silica-rich matrix. Sample HP-3. **d** Centre of a glass pocket, with HIM spherules and ulvöspinel (*usp*), titanium aluminosilicate (*Ti*) and unidentified minerals. Sample KP-9. **e** Anorthoclase-hosted HIM globule, partly displaced along a crosscutting crack (*arrow*). Sample PI-12. **f** HIM globule sealed in zircon (*zrc*). Sample PI-12. **g** SEM image of f) with silicic glass (*black*) coating HIM globule (*grey*). Black areas at the HIM surface are cavities. See analysis #22, Table 3. **h** Primary inclusions of coexisting immiscible HIM (*solid arrows*) and silicic (*open arrows*) melts in the core of the zircon shown in f) and g). Black solids in some inclusions are magnetite daughter minerals

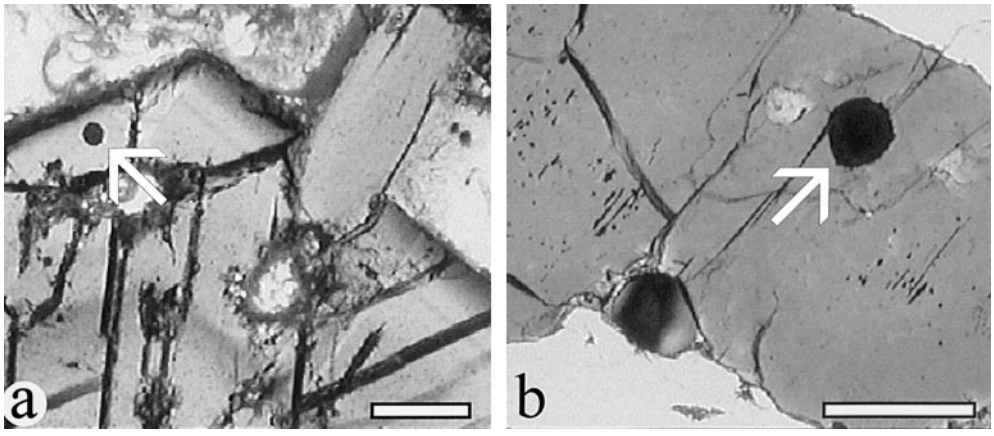

Fig. 3a, b HIM in am-plg gabbroic xenoliths. **a** Globule of TiO_2-enriched glass trapped in growth-zone of euhedral amphibole. Sample HO-1 (Hodejov). **b** Iron-oxide dominated HIM globule trapped in anhedral post-cumulus amphibole. Oriented small black grains within amphibole are ilmenite inclusions. Sample HP-1 (Pinciná). Scale bars represent 200 μm

Only transparent portions of the glass pockets devoid of HIM and impurities were used for analysis. The silicic glasses KP-9 and KP-31, however, may contain impurities (HIM and/or minerals). The mineral and glass separates were powdered in an agate mortar, immersed in a mixture of 3 ml HF and 3 ml $HClO_4$, and heated for 14 hours at 180 °C in a screw-top teflon capsule. The solution was evaporated to dryness at 160 °C, dissolved in 10 ml (HIM) or 50 ml (Si-glass, plagioclase) of 2% HNO_3 and spiked with 20 ppb In. The analyses were performed with a PLASMAQUAD PQ2+ spectrometer at 1350 Watt power in peak jump mode with 10.24 ms dwell time and three measurements per peak. The conjugate phases were measured in one block, along with blank, calibration solutions and standards. The calibration solutions were prepared from certified standard solutions (ALPHA). International rock standards JA-2 and JB-3 were used for correction. Accuracy of the analyses is better than 20% for concentrations <1 ppm, 10% for those between 1 and 100 ppm, and 5% for those above 100 ppm.

For oxygen isotope analysis, fragments of pure minerals and glasses, 1–2 mm in size, were cleaned in a 5% HCl solution in an ultrasonic bath to remove surface-bonded impurities. The glass and mineral grains were evaporated in fluorine with a KrF-based excimer laser (Wiechert and Hoefs 1995). The liberated oxygen was converted to CO_2 over red-hot diamond and measured on-line. Oxygen isotope ratios of the glass were checked with the conventional technique on 20 mg duplicate splits by reaction with ClF_3. Differences between the two preparation techniques are about ± 0.1‰. Plagioclases were treated by conventional fluorination, as the laser preparation led to systematically lower $\delta^{18}O$ values, probably due to low yields and/or undefined reaction with the fluorine in the reaction chamber prior to laser treatment.

For hydrogen isotope analysis, 50–100 mg of amphibole or glass was loaded into a molybdenum capsule, dessicated for 24 h at 110 °C and inductively heated at ~1300 °C in an evacuated quartz tube. The liberated water was converted to hydrogen by reaction with uranium at 850 °C and adsorbed onto activated charcoal in a cold trap. Oxygen and hydrogen isotope ratios were measured with a FINNIGAN MAT 251 mass spectrometer and expressed in δ notation as ‰ deviation from V-SMOW. Estimated errors of the δD and $\delta^{18}O$ values are ±1 and ±0.1‰, respectively.

Fluid inclusions were studied in 0.2 mm-thick-slides polished on both sides. Temperatures of phase transitions (final melting and total homogenization) were measured on a LINKAM THMS-600 stages mounted on a NIKON Optiphot-2 (Geological Survey, Bratislava) or OLYMPUS BH-2 microscopes (Comenius University, Bratislava). The NIKON Mplan100 long-working-distance objective with ×100 magnification and the JVC TK-1280E colour CCD camera coupled with VIDEOBLASTER™, CREATIVE LABS Inc. interface permitted observations of phase transitions in the CO_2 inclusions as small as 1–3 μm in diameter on a computer screen. The freezing-heating stages were calibrated according to melting points of standard chemical compounds and phase transitions in synthetic fluid inclusions. Absolute error of the temperature determinations is ±0.1 °C. Densities and isochores for the CO_2 inclusions were recalculated from the equations of state (Angus et al. 1976; Sterner and Pitzer 1994).

Room temperature ^{57}Fe resonant-absorption Mössbauer spectra were obtained at the Slovak Technical University, Bratislava, from 10–20 mg of hand-picked glass fragments, 0.3–0.5 mm in size, in transmission geometry using a constant acceleration standard spectrometer IMA (Hungary). ^{57}Co in Rh matrix was used as a source of gamma radiation. Least -square fit of the experimental data was performed using a NORMOS computer program. The $Fe^{3+}/\Sigma Fe$ ratio in the glass was derived from the spectra as the ratio of the Fe^{3+} doublet area relative to the total absorption envelope. Oxygen fugacities ($\log f_{O_2}$) were recalculated from the empirical equation correlating temperature, Fe^{2+}/Fe^{3+}, $Al^{3+}/Al^{3+} + Si^{4+}$, $Fe^{3+}/Fe^{3+} + Si^{4+}$ ratios, and NBO/T values for the network-modifying cations in the silicate glasses (Mysen and Virgo 1989; Mysen 1991).

Silicic glass and HIM globules were characterized by Fourier transformation infrared microspectroscopy (FT-IR). The spectra were obtained in transmission mode using an IFS 55 BRUKER spectrometer linked to a BRUKER microscope (Barrés et al. 1987) at the LEM-UA CNRS 235 laboratory (Nancy, France). A MCT detector allows detection of fundamental vibrations in the mid-infrared range with a 4 cm^{-1} spectral resolution. The size of the analyzed circular area can vary from 8 to 150 μm in diameter using ×15 and ×36 objectives. For this study, ×15 objective with 80 μm aperture has been chosen, considering inclusion size. Doubly polished slides designed for microthermometry and single HIM fragments extracted from plagioclases were used for acquisition of the FT-IR spectra. The samples were put on a fluorite (CaF_2) slide, transparent in the mid-infrared region (4500–800 cm^{-1}). The IR spot was controlled by visible observation of the focused zone. Contribution of atmospheric CO_2 and H_2O was eliminated by subtraction of independently recorded spectra from that of the analysed sample.

Results

Chemical properties of melts

Syenitic xenoliths

Compositions of HIM-bearing silicic glass pockets within the syenitic xenoliths correspond to trachyte in the total alkalis versus silica (TAS) diagram (Fig. 5). Brown-coloured parts of the melt pockets are 2–3 wt% enriched in FeO_{tot} relative to transparent ones. Residual glass in zircon-hosted multiphase melt inclusions is also

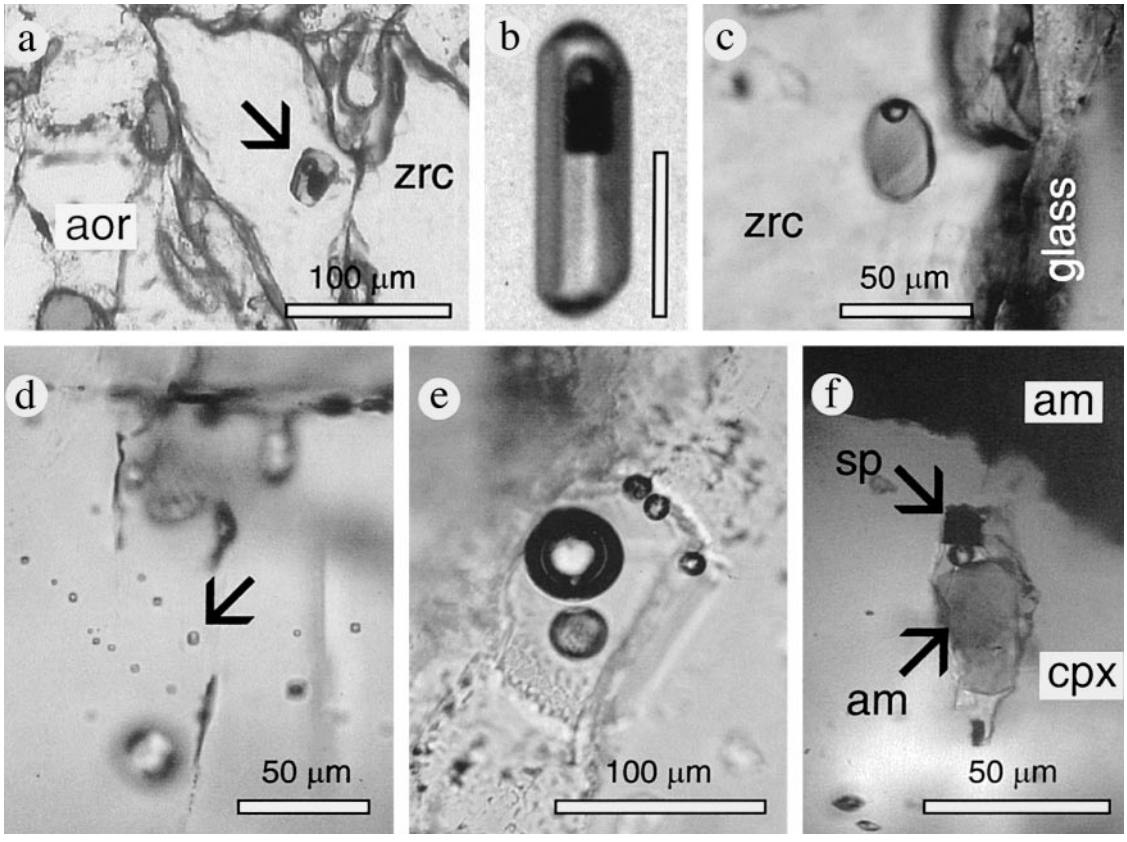

Fig. 4a–f Inclusion fluids in HIM-bearing syenitic (a–e) and gabbroic (f) xenoliths. **a** Primary, polyphase melt inclusion in a large resorbed zircon (*zrc*) encompassed by anorthoclase (*aor*). Opaque daughter mineral in the inclusion is magnetite. Sample HP-3. See analyses #49 and #52, Table 3. **b** Tubular melt inclusion trapped in zircon which consists of 3 vol.% vapour, 7 vol.% of magnetite and 90 vol.% of residual trachytic glass. Bar scale corresponds to 10 μm. Sample HP-3. **c** Two-phase melt inclusion trapping a homogeneous melt in the marginal part of a zircon. Sample KP-9. **d** Primary, negative crystal-shaped CO_2-rich inclusions in anorthoclase. Sample PI-12. **e** Anorthoclase-hosted primary melt inclusion showing re-equilibration textures: cracks emanating from the inclusion and multiple vapour bubbles result from an increase of the inclusion volume accompanied by partial loss of inclusion melt. Sample KP-9. See analysis #22, Table 3. **f** Clinopyroxene-hosted, polyphase melt inclusion with daughter crystals of Fe, Ti, Mg-spinel (*sp*), amphibole (*am*), residual homogeneous glass and shrinkage bubble. The approximate volumetric phase ratios are sp5/am60/glass35. See analyses #54, #54a and #54b in Table 2

trachytic, overlapping in composition with the pocket glasses (Fig. 5). However, the bulk composition recalculated from the magnetite/glass phase ratio in a regular inclusion (Fig. 4b) corresponds to sodic trachyandesite-to-benmoreite with about 11 wt% FeO. In contrast, compositions of two-phase melt inclusions, particularly those hosted by K-feldspar in sample KP-9 (Fig. 4e), are more felsic, corresponding to trachyte or alkali rhyolite.

^{57}Fe resonant-absorption Mössbauer spectra of the silicic glass pockets (Fig. 6, Table 5) permit the distinction of two groups of syenitic xenoliths. Low Fe^{3+} contents are observed in samples HP-3 and PI-12, in which HIM globules occur in rock-forming minerals and interstitial glasses, whereas higher Fe^{3+} contents are typical of samples KP-9 and PI-14 where HIM spherules are found solely in the interstitial glass.

The silicic melt trapped in syenites is quartz-normative, peraluminous, occasionally metaluminous, almost fully polymerized, with NBO/T ratio (non-bridging oxygens / tetrahedrally coordinated cation) lower than 0.171 (Table 6). The coexisting HIM is essentially similar in all syenitic xenoliths, with SiO_2 ranging from 8 to 11 wt%, FeO_{tot} between 63–68 wt% and small amounts of other oxides, including TiO_2. Up to 20 wt% of volatiles might be indicated by low totals of the electron microprobe analyses (Tables 2–4).

Fourier Transformation Infrared (FT-IR) spectra of the HIM and coexisting Si-rich glass (Fig. 7) reveal molecular water and hydroxyl (OH) groups which is indicated by stretching vibrations between 2800 and 3750 cm^{-1}, H-OH bending at 1650 cm^{-1}, and a steep slope of absorbance curves around 3600 cm^{-1}. Water speciation in the HIM differs markedly from that of goethite or limonite, which exhibit water-related bands at 3140–3100 cm^{-1} accompanied by weak bands at 1630 and 3430 cm^{-1} and no vibrations near 3700 cm^{-1} (Van der Marel and Beutelspacher 1976). We thus conclude that hydration of the HIM and coexisting Si-rich glass is a magmatic feature, because the melts encapsuled in fresh, non-metamict zircon (Fig. 2f–h) appear to be unaffected by secondary, low-temperature hydration.

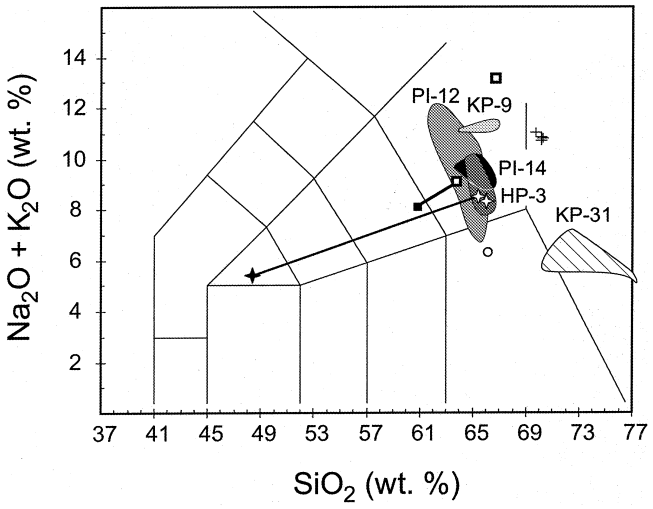

Fig. 5 Total alkalis vs silica (TAS) diagram (LeMaitre 1989) with syenite- (*shaded areas*) and granite-hosted (*diagonally striped area*) interstitial, silicic glasses and inclusion melts trapped in zircon (*squares*), anorthoclase (*crosses*), and clinopyroxene (*stars*). *Solid symbols* are compositions of bulk melts reconstructed from crystal/melt phase ratios in individual inclusions. *Coupled open symbols* are projection points of the residual glass within the polyphase inclusions. Sample numbers correspond to syenite (KP-9, PI-12, HP-3, PI-14), granite (KP-31) and am-plg cumulate (HP-1)

More or less intense absorption in the 1415–1450 cm^{-1} range was observed in the HIMs, which is especially true for sample PI-12 (Fig. 7) and less pronounced for sample HP-3. This contrasts with coexisting silicic glasses, which were always inactive in this range. The 1415–1450 cm^{-1} band can be assigned to CO_3^{2-} stretching, organic contribution or NH_4 bending vibration. The first possibility seems to be the most probable, because neither organic compound-related C-H stretching vibrations at 3000–2800 cm^{-1}, nor a 3300–3000 cm^{-1} contribution associated with NH_4 have been observed. There was no evidence for molecular CO_2 in the samples studied.

Location of the CO_3^{2-} peak is identical with the position of the CO_3^{2-} asymmetric stretch vibration of carbonate minerals. The single band, however, contrasts with the CO_3^{2-} doublet commonly observed in synthetic and natural glasses (e.g., Blank and Brooker 1994; Grzechnik et al. 1996). The doublet composed of two peaks at 1400 and 1500 cm^{-1} is assigned to V_3 antisymmetric vibration modes of distorted carbonate groups. The doublet would reduce to a single peak at 1415 cm^{-1} if all C-O bonds were equivalent (Fine and Stolper 1985).

Granitic xenoliths

Interstitial melt in the granitic xenolith KP-31 corresponds to medium-K, sub-alkalic rhyolite in the TAS diagram (Fig. 5). It has essentially the same composition as the inclusion glass in hypersthene. It grows from the interstitial melt together with ilmenite, proving coexistence of all three phases (Table 4). The silicic glass is highly polymerized (NBO/T = 0.041), with a $Fe^{3+}/\Sigma Fe$ ratio of only 0.01 (Tables 5, 6).

Gabbroic (am-plg) xenoliths

Primary silicate melt inclusions associated with the HIM have been found only in the amp-plg xenolith

Fig. 6 ^{57}Fe Mössbauer resonant absorption spectra of silicic interstitial glass from low Fe^{3+} (HP-3) and high Fe^{3+} (PI-14) syenitic xenoliths

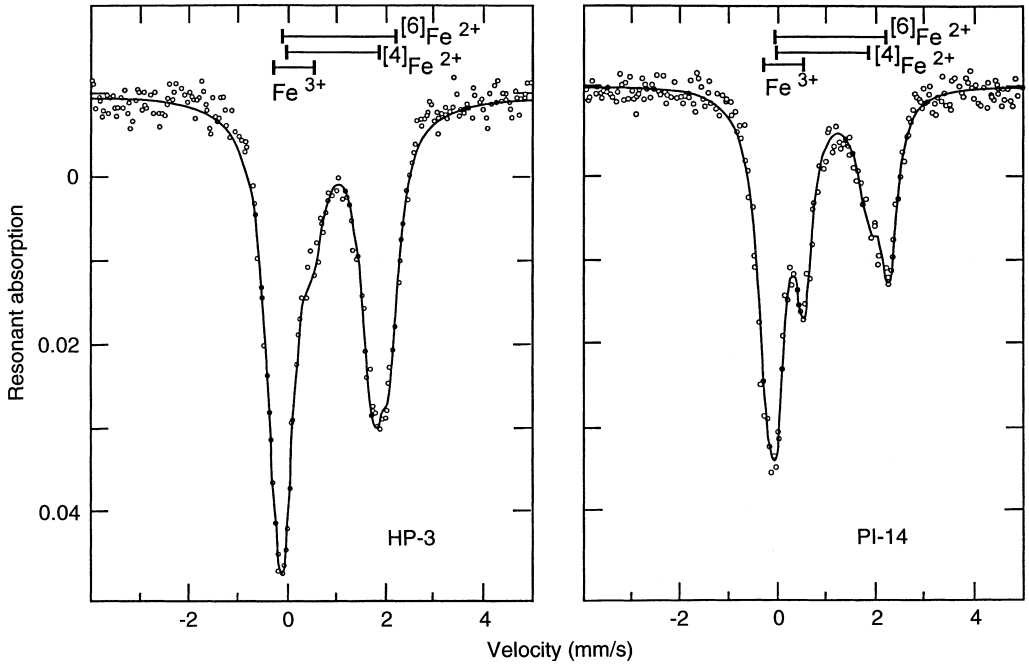

Table 5 Hyperfine parameters and Fe^{3+}/Fe^{2+} ratios in silica-rich interstitial glasses estimated by ^{57}Fe Mössbauer spectroscopy (see Fig. 6 for comparison)[a]

	$\Delta_1 Fe^{2+}$			$\Delta_2 Fe^{2+}$			ΔFe^{3+}		
	IS (mm/s)	QS (mm/s)	A (%)	IS (mm/s)	QS (mm/s)	A (%)	IS (mm/s)	QS (mm/s)	A (%)
HP-3	1.02	2.27	29.2	0.91	1.80	55.5	0.17	0.80	15.3
PI-12	1.05	2.43	48.6	0.98	1.80	34.9	0.17	0.80	16.5
KP-9	1.12	2.38	34.2	1.00	1.94	30.7	0.16	0.85	35.1
PI-14	1.14	2.31	31.3	0.96	1.90	29.9	0.17	0.80	38.8
KP-31	1.03	2.21	60.2	0.95	1.75	31.4	0.17	0.80	8.4

[a] *IS* isomer shift, *QS* quadrupole split, *A* peak area

Table 6 Anhydrous CIPW-normative compositions, structural properties and oxygen fugacities of interstitial (syenitic and granitic xenoliths) and inclusion-hosted silicic melts (am-plg xenolith) coexisting with HIM

Sample No.	HP-3 (∅5)	PI-12 (∅14)	KP-9 (∅2)	PI-14 (∅5)	KP-31 (∅5)	HP-1
Xenolith	Syenitic				Granitic	Am-plg
CIPW norms[a]						
Quartz	11.18	10.33	7.01	12.43	41.18	–
Orthoclase	26.44	27.98	30.52	22.12	16.15	9.94
Albite	39.22	43.44	51.72	47.92	22.90	30.01
Anorthite	7.87	3.28	3.87	4.83	6.31	22.90
Nepheline	–	–	–	–	–	0.32
Corundum	–	4.78	2.47	4.60	2.75	–
Diopside	4.99	–	–	–	–	8.57
Hypersthene	6.66	6.70	3.45	3.66	4.52	–
Olivine	–	–	–	–	–	15.37
Magnetite	1.46	0.97	1.62	2.06	0.42	4.44
Ilmenite	0.23	0.17	–	0.23	1.65	6.18
Apatite	0.04	0.13	–	0.04	0.55	0.68
Structural parameters						
ΣNBO/T	0.171	0.035	0.006	–	0.041	0.675
$(NBO/T)^{Ca}$	0.028	0.001	0.001	–	0.001	0.067
$(NBO/T)^{Mg}$	0.002	0.009	0.002	–	0.021	0.300
$(NBO/T)^{Fe^{2+}}$	0.113	0.008	0.003	0.007	0.012	0.209
$(NBO/T)^{Fe^{3+}}$	0.028	0.018	–	–	0.007	0.100
Sheets (T_2O_5)	0.025	0.008	0.003	0.007	0.012	0.010
Chains (TO_3)	0.047	–	–	–	–	0.208
Dimers (T_2O_7)	–	–	–	–	–	0.007
Monomers (TO_4)	0.006	–	–	–	–	0.033
3D (TO_2)	0.921	0.991	0.994	0.988	0.978	0.704
$Al/Al+Si(TO_2)$	0.236	0.270	0.261	0.271	0.172	0.404
$Al/Al+Si(T_2O_5)$	0.118	0.135	0.131	0.135	0.086	0.202
Oxygen fugacities						
$Fe^{3+}/\Sigma Fe$	0.153	0.165	0.351	0.388	0.099	0.245
$\log f_{O_2}$[b]	−13.97	−13.50	−12.24	−12.09	−14.07	−13.61
Std. error	±1.42	±1.54	±1.37	±1.38	±1.21	±1.79
$\log f_{O_2}$-QFM	−1.32	−0.84	0.47	0.57	−1.42	−0.95

[a] Recalculated from chemical analyses in Tables 2–4
[b] Normalized to 900 °C and 1 bar

HP-1, within clinopyroxene nucleation centres of amphibole oikocrysts. The polyphase melt inclusions contain a vapour bubble, one large amphibole, one or two small spinels and residual trachytic glass (Fig. 4f), which is similar in composition to the syenite pocket melt (Fig. 5). Bulk composition of the inclusion melt recalculated from chemical analyses and volumetric ratios of the inclusion phases (Table 2) corresponds to trachybasalt (Fig. 5). The residual inclusion melt contains only negligible FeO_{tot} ranging from 0.0–0.3 wt% (Table 2). It is therefore possible to recalculate bulk Fe^{3+} content of the melt from stoichiometry and volumetric ratios of the daughter amphibole and spinel. Corresponding anhydrous CIPW norms, structural properties and relative oxygen fugacities are listed in Table 6. An alkaline, quartz-undersaturated character

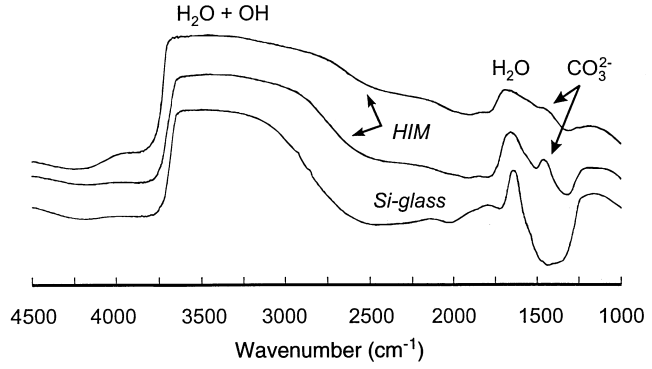

Fig. 7 Fourier transformation infrared spectra of HIM and silicic interstitial glass from syenite PI-12

of the parental trachybasalt is indicated by nepheline in the norm.

HIM globules have been observed within the silicic melt inclusions hosted by cpx or as single globules trapped along growth planes of the cumulus cpx and post-cumulus kaersutite. There are no significant compositional differences between the cpx- and am-hosted HIMs in terms of SiO_2 and FeO_{tot} contents (Table 2). Generally, however, SiO_2 tends to increase from gabbroic (6 wt%), through syenitic (8–11 wt%) to granitic xenoliths (24 wt%), while FeO_{tot} appears to be inversely proportional to SiO_2. In contrast to the Pinciná locality, the HIM from am-dominated cumulate of Hodejov is strongly enriched in TiO_2 (43.5 wt%) and depleted in FeO_{tot} (10.6 wt%). The water-attributed deficiency in the totals of the microprobe analyses, correlating with the FeO_{tot}, might be suggestive of an Fe-OH bonding in the HIMs.

CO_2-inclusion microthermometry

Preliminary microthermometry data on CO_2 inclusions have already been published and discussed by Huraiová et al. (1996). Here we provide a refined and extended set of measurements for syenitic xenoliths, as well as that for the HIM-hosted gabbroic xenolith HP-1. In order to minimize effects of re-equilibration, only negative crystal-shaped inclusions, 1–3 μm in diameter, have been selected for microthermometry in feldspars.

Two groups of syenitic xenoliths were defined by CO_2 homogenization temperatures (T_h) clustering typically at 27–31 °C and 3–10 °C (Fig. 8, upper left-hand histogram). Corresponding densities are between 0.68–0.66 and 0.90–0.87 g/cm^3, respectively. Maximum densities in both groups are likely to approach the actual fluid densities, whereas the less dense CO_2 may result from inclusion volume modifications (stretching, decrepitation) of the inclusions. CO_2 melting temperatures are

Fig. 8 Temperatures of homogenization (*top*) and last melting (*bottom*) in primary CO_2-rich inclusions hosted in syenitic xenoliths (*left*) and amphibole-plagioclase cumulate HP-1 (*right*). S, L, G denote solid, liquid, and gas phases, respectively

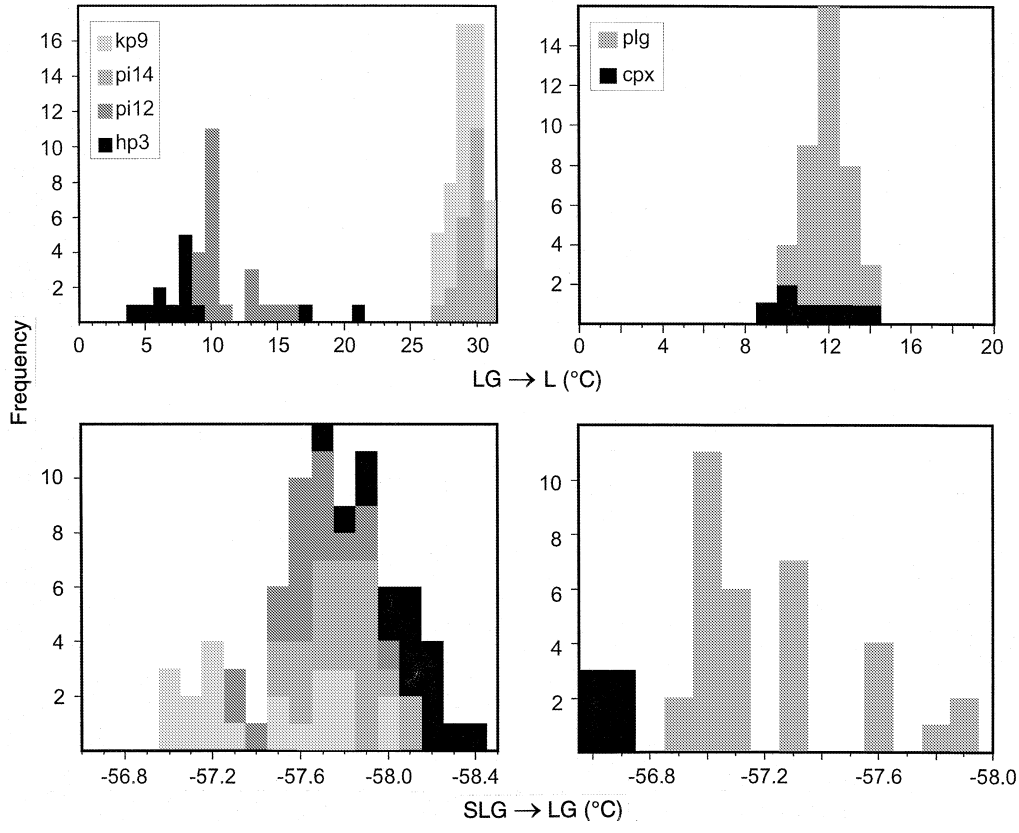

consistently below −56.6 °C – the triple point for pure CO_2 (Fig. 8, lower left-hand histogram), and thus indicate additional gas compounds. This is indirectly corroborated by critical homogenization around +31.3 °C, i.e. 0.2 °C above the critical point for pure CO_2, observed in larger, partially re-equilibrated inclusions. The two groups of syenitic xenoliths discriminated according to contrasting CO_2 densities are identical with those distinguished on the basis of the different $Fe^{3+}/\Sigma Fe$ ratio in the interstitial melt.

Fluid inclusions in the am-plg xenolith HP-1 exhibit consistent T_h values in cumulus cpx and post-cumulus Ca-plg (Fig. 8, upper right-hand histogram). The T_m values in the cpx-hosted inclusions are fixed between −56.6 ° and −56.7 °C, corresponding to almost pure CO_2. In contrast, scatter of the T_m values in plagioclase from −56.6 °C to as low as −57.9 °C (Fig. 8, lower right-hand histogram) is suggestive of minor amounts of additional gas components.

Oxygen and hydrogen isotope data

Oxygen and hydrogen isotope ratios in major xenolith phases are listed in Table 7. The $\delta^{18}O$ values of zircons from synitic xenoliths (5.1–5.6‰) are identical with those of mafic minerals and calcic plagioclase (4.9–5.9‰) from the gabbroic xenoliths, and are in agreement with a common mantle source for these rocks. Since oxygen diffusion rates in zircon are extremely low under water-absent conditions (Valley et al. 1994; Watson and Cherniak 1997), it is assumed that zircon in the syenitic xenoliths has retained its mantle isotopic signature of the parental trachyandesite melt, and has not been modified by interaction with crustal fluids. Hydrogen isotope ratios between −61 and −86‰ of the gabbroic kaersutite are consistent with the δD range commonly accepted for mantle-derived, primary magmatic water (Hoefs 1997).

Isotope exchange with crustal fluids or melts may account for the increase of $\delta^{18}O$ values in alkali feldspar (6.3–7.3‰), quartz (9.0‰) and silicic glass (6.7–9.9‰) of the felsic xenoliths, inasmuch as an ^{18}O-enrichment in excess of 1‰ cannot be achieved during magmatic crystal fractionation (e.g., Hoefs 1997). Extremely light hydrogen isotope data in water extracted from the trachyte (−107‰) and rhyolite (−134 and −142‰) glasses may be caused by molecular water-OH fractionation during sample preparation (e.g., Ihinger et al. 1994), or more likely may result from a natural outgassing (Dobson et al. 1989). An interaction with meteoric water can be ruled out, because the glasses and associated plagioclases do not show any sign of an ^{18}O depletion.

Trace element patterns

Trace element abundances have been determined for the silicic interstitial glasses of the felsic xenoliths. For the coexisting HIM, trace element contents and corresponding distribution coefficients have been estimated in the low Fe^{3+} syenites HP-3 and PI-12 (Table 8).

Trace element patterns are very similar for the syenitic and granitic xenoliths (Fig. 9). Strong enrichment in Th, Nb and Ta indicates the highly evolved nature of the melts. An extremely high Nb content of 1400 ppm in the syenite KP-9 is attributed to the presence of small amounts of Nb-bearing minerals.

The conjugate HIM and silica-rich melts are strongly depleted in Sr and Eu due to feldspar crystallization (Fig. 10). More pronounced Eu anomalies in the low Fe^{3+} syenites HP-3 and PI-12 (Eu/Eu* = 0.14–0.24) compared with elevated Eu/Eu* values (0.21–0.31) for the high Fe^{3+} syenites (KP-9, PI-14) point to different redox conditions during formation of the two syenite groups.

P-T-f_{O_2} conditions during HIM separation

Equilibrium PT conditions for gabbroic cpx have been estimated at the intersection point of the isopleths according to Lindsley (1983) and Nimis (1995). The Lindsley correction scheme for non-quadrilateral components was modified by incorporating a correction to TiCa-Tschermak's molecule, leading to a decrease of the

Table 7 Oxygen and hydrogen isotope ratios in rock-forming minerals and melts

Sample No.	Xenolith	Ol	Cpx	Sp	Am		Plg	Qtz	Zrc	Glass	
		$\delta^{18}O$	$\delta^{18}O$	$\delta^{18}O$	$\delta^{18}O$	δD	$\delta^{18}O$	$\delta^{18}O$	$\delta^{18}O$	$\delta^{18}O$	δD
KP-31	Granitic						–	–		9.2	−134
KP-30	Granitic						7.7	9.0		9.5	−142
KP-9	Syenitic						7.2		5.6	9.9	–
PI-14	Syenitic						7.1		–	–	–
PI-12	Syenitic						7.3		5.1–5.5	7.1	–
HP-3	Syenitic						6.3		–	6.7–6.9	−107
HP-1	Am-plg cumul.				4.9	−85	5.9				
HP-4	Am-plg cumul.				5.7	−64	–				
PI-19	Am-plg cumul.				5.2	−65	5.6				
PI-13	Cpx-plg cumul.	5.1	5.7	5.5	5.4	−86	5.9				
PI-18	Cpx-plg cumul.		–		5.0	−61	5.4				

Table 8 Trace element contents (ppm) in HIM and the coexisting silicic glass, and corresponding partition coefficients, $K_{d\theta}$ (*nd* = not determined)

Xenolith	Syenitic									Granitic
No.	HP-3			PI-12			KP-9	PI-14 (Si-glass)		KP-31
Phase	HIM	Si-glass	K_d	HIM	Si-glass	K_d	Si-glass	Transp.	Black	Si-glass
Li	1.6	19	0.08	7.4	26	0.28	5.3	16	12	8.2
Be	2.4	2.4	1	7.6	4.8	1.6	1.9	8.4	4.6	1.4
Rb	10	110	0.09	65	340	0.19	79	100	96	63
Sr	110	65	1.7	100	27	3.8	56	36	35	260
Cs	1.5	4.5	0.33	1.3	4.6	0.28	1.9	2.9	2.5	1.2
Ba	180	240	0.75	190	109	1.7	790	290	380	580
Pb	3.6	10	0.36	11	11	1	6.9	17	10	12
Th	2.1	14	0.15	23	17	1.3	3.8	11	21	31
U	1.7	2.9	0.59	5.6	3.8	1.7	0.61	9.8	14	2.4
Sc	43	2.0	22	16	1.1	14	2.6	0.06	1.9	4.7
V	300	17	17	92	6.0	15	nd	nd	nd	63
Cr	300	25	12	200	39	5	3.8	0.00	0.08	12
Co	540	2.4	220	200	2.0	100	19	1.1	3.9	9.7
Ni	2600	20	130	1960	14.1	140	57	3.8	16.6	11
Zn	1700	140	12	1250	120	11	nd	nd	nd	87
Cu	500	4.8	100	1100	8.9	120	nd	nd	nd	7.0
Mo	180	3.5	50	42	2.5	17	8.7	3.7	1.6	0.39
Y	52	37	1.4	51	16	3.3	6.4	6.4	12	15
Zr	280	740	0.38	260	230	1.1	47	240	200	240
Hf	4.2	14	0.30	4.2	4.1	1	1.1	8.0	5.6	7.0
Nb	290	73	3.9	230	162	1.4	1400	160	121	57
Ta	13	2.9	4.5	54	28	2	48	7.4	18	2.5
Sn	7.1	2.9	2.5	13	4.3	3.1	1.7	3.5	2.6	1.9
W	1.1	1.1	1	3.3	1.2	2.7	0.57	1.1	0.97	0.16
La	55	160	0.34	79	120	0.66	36	12	14	92
Ce	86	250	0.34	120	170	0.71	41	56	33	130
Pr	9.3	22	0.42	15	14	1.07	7.7	2.4	3.1	16
Nd	36	70	0.51	49	41	1.20	22	6.9	9.0	53
Sm	6.8	10	0.68	8.1	4.7	1.72	2.8	1.1	1.5	7.5
Eu	1.5	1.7	0.88	1.0	0.74	1.35	0.76	0.21	0.44	1.2
Gd	6.4	7.3	0.88	6.5	3.2	2.03	2.1	0.97	1.6	5.0
Tb	1.1	1.0	1.10	1.1	0.42	2.62	0.26	0.14	0.28	0.61
Dy	6.7	5.9	1.14	6.6	2.2	3.00	1.2	0.91	1.8	3.0
Ho	1.4	1.2	1.17	1.6	0.48	3.33	0.24	0.22	0.44	0.54
Er	4.1	3.6	1.14	4.7	1.4	3.36	0.65	0.78	1.4	1.6
Tm	0.69	0.65	1.06	0.88	0.25	3.52	0.09	0.16	0.23	0.22
Yb	5.1	5.6	0.91	6.4	2.0	3.20	0.64	0.95	1.7	1.6
Lu	0.96	1.2	0.80	1.1	0.35	3.14	0.11	0.14	0.23	0.27

final temperature by about 100 °C. The inferred values represent minimum *T* and maximum *P*, because of the absence of orthopyroxene in the assemblage and due to a slightly negative slope of the isopleths derived from Nimis. The inferred temperatures are probably accurate within 70–100 °C, owing to uncertainties in the isotherms and 10–15 mol% of non-quadrilateral components in the cpx studied (Lindsley 1983). Uncertainty of the pressure estimates appears to be within ±1.5 kbar (Nimis 1995).

Equilibrium *PT* conditions for the HIM-hosted cpx from am-plg gabbroic xenolith HP-1 are 1080–1180 °C and 7.3–9.6 kbar. Isochores for the densest CO_2 inclusions (0.86 g/cm^3) project to 5.5–6 kbar, suggesting that the inclusion volumes have been modified due to internal overpressure (decrepitation). Re-equilibration mode is indicated by the planar shape of cracks around the inclusions, and the crack lengths proportional to inclusion sizes – the textures typical of isothermal decompression (Sterner and Bodnar 1989; Vityk and Bodnar 1995; Vityk et al. 1996).

The Ti-in-hornblende thermometer (Otten 1984) yields temperatures of 1000–1010 °C for the HIM-hosted amphibole cumulate from Hodejov (HO-1) and 1010–1050 °C for amphibole-plagioclase cumulate from Pinciná (HP-1). Deduced from densities of the CO_2 inclusions trapped in coexisting Ca-plg, fluid pressures at Pinciná could have reached 5–5.4 kbar. In contrast to cpx, the inclusions in plagioclase are believed to record true trapping pressures due to the absence of re-equilibration textures (no planar cracks around small inclusions) and consistency of the obtained homogenization temperatures (Fig. 8).

Crystallization temperatures of the syenitic xenoliths are not well-constrained. Melt inclusion-based thermometry failed due to decrepitation and stretching of feldspar at higher temperatures (Huraiová et al. 1996). Relatively high temperatures >900 °C – typical

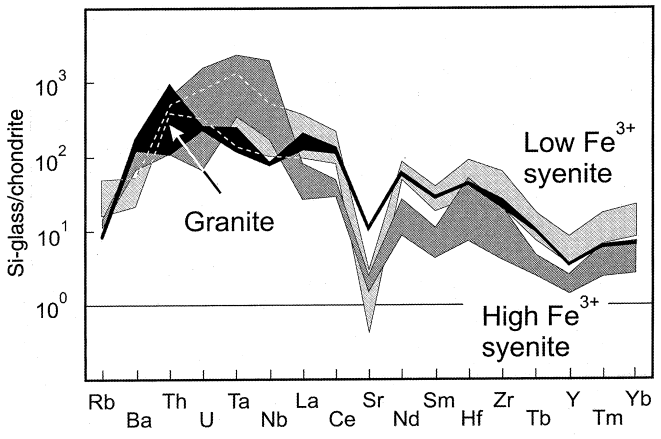

Fig. 9 Chondrite-normalized (Anders and Grevesse 1989) spider diagrams of interstitial silica-rich glasses from granitic and syenitic xenoliths. Especially noteworthy is the negative Sr anomaly due to feldspar fractionation

of water-deficient alkali granite – are indicated by simple zircon morphology (combinations of first-order pyramidal {101} and prismatic {100} forms, Pupin 1980). Assuming crystallization T around 900 °C, corresponding CO_2 inclusion pressures would reach 2.8–2.9 kbar for the high Fe^{3+} syenites (KP-9, PI-14) and 4.8–5.2 for the low Fe^{3+} syenites HP-3 and PI-12, equivalent to depths around 12–13 and 18–19 km, respectively.

Contrasting $Fe^{3+}/\Sigma Fe$ ratios in the two syenite horizons may reflect two distinct batches of fractionating magma, various degrees of devolatiliziation, or a pressure-dependent control on the $Fe^{3+}/\Sigma Fe$ ratio (Mysen and Virgo 1978, 1985; Mysen 1991). The covariations among the Eu/Eu* values, the depression of final melting temperatures of the CO_2 inclusions (Fig. 8), and the different onset of the HIM separation, however, seem to exclude secondary processes, such as devolatilization and/or subsurface fluid-rock interaction, which could also potentially affect the primary Fe^{3+} content of the melt.

Normalized log f_{O_2} values recalculated from melt structure parameters and $Fe^{3+}/\Sigma Fe$ ratios (Mysen and Virgo 1989) project 0.8–1.3 log units **below** the quartz-fayalite-magnetite buffer (Frost 1991) for the low Fe^{3+} syenites and 0.5–0.6 log units **above** QFM for the high Fe^{3+} ones (Table 6). The contrasting log f_{O_2} values, coincidental with the depression in CO_2 melting temperatures, argue for the presence of reducing gas species, such as methane and/or carbon monoxide in the magmatic fluids, accompanying the CO_2 during a late-stage differentiation in the magma chamber.

Crystallization PT conditions of granitic xenoliths cannot be convincingly elucidated. Densities of the inclusion CO_2 (0.85 g/cm^3) and the low Fe^{3+} content of

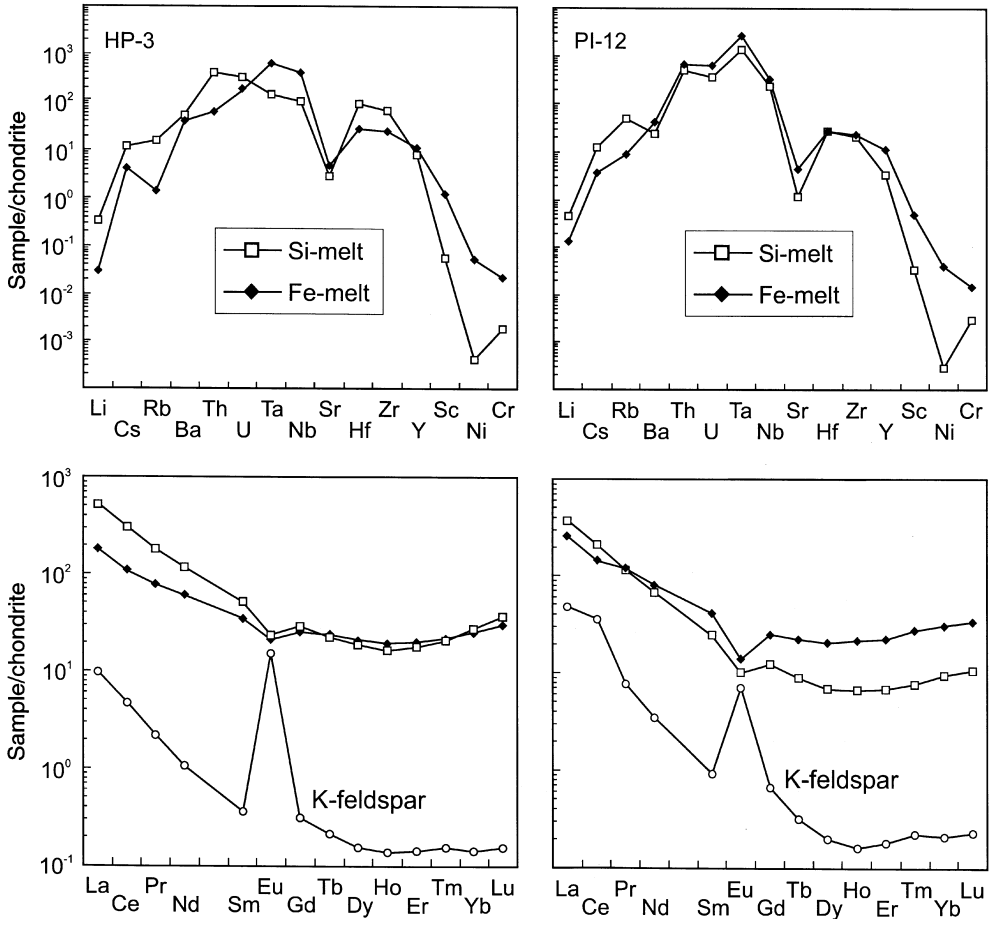

Fig. 10 Chondrite-normalized (Anders and Grevesse 1989) multi-element spidergrams of conjugate HIM and Si-rich melts, and coexisting K-feldspar from low Fe^{3+} syenites. The negative Sr and Eu anomalies in conjugate melts point to a magmatic origin of the HIM

interstitial melt (Tables 5, 6) in the granite KP-31 are similar to those of the deep-seated, more reducing syenites. Primary silicate melt inclusions in quartz yielded homogenization temperatures in excess of 1000–1100 °C (Huraiová et al. 1996). At these temperatures, corresponding fluid pressures would match those derived for the deep-seated, low Fe^{3+} syenites.

Discussion

Origin of xenoliths

Several lines of evidence suggest that the kaersutite- and clinopyroxene-dominated gabbroic xenoliths originated by crystal accumulation from silica-undersaturated alkali basalt:

- Ti-enriched and Al, Si-deficient character of amphibole
- absence of orthopyroxene in the mineral assemblage
- alkali trachybasalt composition of primary melt inclusions in clinopyroxene
- mantle isotopic signature of all minerals, including Ca-plagioclase, with $\delta^{18}O$ values ranging from 4.9 to 5.9‰
- δD values of post-cumulus amphibole between −61 and −86‰, characteristic of primary magmaic water
- CO_2-dominated, water-absent primary fluid inclusions
- maximum pressures during cpx crystallization corresponding to recent upper mantle conditions.

The syenitic xenoliths seem to represent products of alkali basalt fractionation within the crust. The following arguments support this assumption:

- mantle isotopic signature of zircon (5.1–5.6‰)
- CO_2-rich, water-absent inclusion fluids
- inclusion fluid pressures indicating middle-to-deep crustal conditions.

Mineral assemblages of the gabbroic and syenitic xenoliths described in this and companion papers (Huraiová et al. 1996) are almost fully consistent with the inventory of megacrysts entrained worldwide in continental alkali basalts and their derivatives. For instance, trace element distributions (e.g., Irving and Frey 1984) have shown that kaersutite and clinopyroxene megacrysts may have been in equilibrium with their host alkali basalts, while anorthoclase, mica and zircon must have crystallized from more evolved liquids, corresponding very likely to benmoreite (Guo et al. 1992) or trachyte (Aspen et al. 1990). According to strontium isotope data, Aspen et al. (1990) attributed generation of the evolved melts to fractionation of partial melts derived from lithospheric mantle.

Origin of the granitic xenoliths is more controversial. Highly reducing interstitial glass, trace element abundances similar to those in syenite, essentially CO_2-dominated primary inclusions and presence of HIM strongly argue for a close genetic relationship with alkali basalts. On the other hand, involvement of a crustal component is supported by:

- enrichment in ^{18}O (up to 9.9‰) of the rock-forming minerals and interstitial glass
- presence of water within CO_2-dominated primary inclusions in one granitic xenolith (KP-30, not included in this study), indicating a crystallization from water-oversaturated melt (Huraiová et al. 1996)
- sub-alkalic character of interstitial rhyolite glass projecting outside the hypothetical liquid line of descent connecting alkali basalt and alkali rhyolite.

Homogenization temperatures of silicate melt inclusions from granitic xenoliths in excess of 1000–1100 °C are quite comparable to a CO_2-saturated, dry (water-absent) solidus of a haplogranite melt, which is located at around 970 °C at 5 kbar (Keppler 1989). A high-temperature (1150 °C) generation of dacite and rhyolite has been reported from experiments of metapelite melting by interaction with high-alumina tholeiitic basalt (McCarthy and Patiño Douce 1997). However, the interstitial rhyolite glass of the investigated xenoliths possesses some features reminiscent of an A-type granite originating by fractionation of basaltic magma: mildly peraluminous composition, anhydrous mafic mineralogy, high LREE content, negative Eu anomaly, highly evolved trace element characteristics and post-orogenic, extension-related tectonic setting (e.g., Turner et al. 1992).

Two-liquid trace element partitioning

Experimental partition coefficients from coexisting ferrobasalt and granite melts are available for a limited set of trace elements. During experiments at 1 atm pressure, most trace elements preferentially concentrate in the Fe-rich melt, whilst Cs and Rb always partition into the silica-rich liquid (Watson 1976; Ryerson and Hess 1978; Ellison and Hess 1989; Vicenzi et al. 1992, 1994; Green 1994). Watson (1976) reported on a weak ionic radius-dependent fractionation among rare earth elements (REE) in doped synthetic glasses, but later experiments have not corroborated such behaviour (Ellison and Hess 1989; Vicenzi et al. 1994). Pressures up to 13 kbar have no significant influence on the trace element partitioning observed at 1 atm, with the exception of Sr and Ba, whose distribution coefficients appear to increase with pressure (Green 1994). The partition coefficient for uranium substantially increases with rising f_{O_2}, while that for thorium remains nearly constant. The divergent behaviour of U and Th was attributed to changing valence state of the uranium under more oxidising conditions. An f_{O_2}-independent, melt compositional control was proposed to account for changing Nb/Ta and Zr/Hf ratios in the coexisting immiscible liquids (Vicenzi et al. 1994).

Trace element partitioning between HIM and trachyte melts is different from that observed in the pyroxene- and quartz-normative melts, although some features remain similar, particularly the affinity of most elements to the iron-rich phase with the exception of Li, Rb and Cs. Fractionation of the transition elements and base metals is especially high, with K_d(Fe/Si) values in excess of 100 for Co, Ni and Cu, and over 5 for Sc, V, Cr and Mo (Fig. 11, Table 8). This leads to extreme enrichment of the HIM which contains up to 0.26 wt% Ni, 0.17 wt% Zn and 0.11 wt% Cu. Notable also is the affinity of Sn to the HIM, although this element is normally expected to prefer silica-rich melts. Nb and Ta have also concentrated in the HIM.

Heavy REE are compared to the light REE enriched in the HIM by a factor of 6. The LREE/HREE ratios are thus perturbed by the process of immiscibility, which produces a residual Si-rich liquid enriched in LREE and depleted in HREE. Apart from this, a specific fractionation does exist also between the medium and heavy REE, as indicated by the maximum K_d(Fe/Si) values corresponding to Tb-Tm, whereas those for Yb and Lu are somewhat lower (Fig. 11, Table 8). Hence, a recurrent immiscible separation of the HIM and its continual extraction from the system by gravitational settling or compaction of a crystal-liquid mush could result in a strong enrichment of the residual silica-rich liquid in La and Ce and concomitant depletion of Tb-Tm compared to Yb and Lu.

In the light of these observations, flat chondrite-normalized distribution curves for the medium and heavy REE of the silicic glass from the high Fe^{3+} syenites and granites can be interpreted to reflect no or little loss of the HIM from the system. This is in accord with the microscopically observed onset of immiscibility, postdating crystallisation of rock-forming minerals in these xenoliths. In contrast, a weak fractionation among medium and heavy REE in the Si-rich melts from low Fe^{3+} syenites (Fig. 10), is interpreted as resulting from extraction of the HIM from the magmatic system. This is consistent with the microscopic observations of immiscible separation contemporaneous with the mineral crystallization.

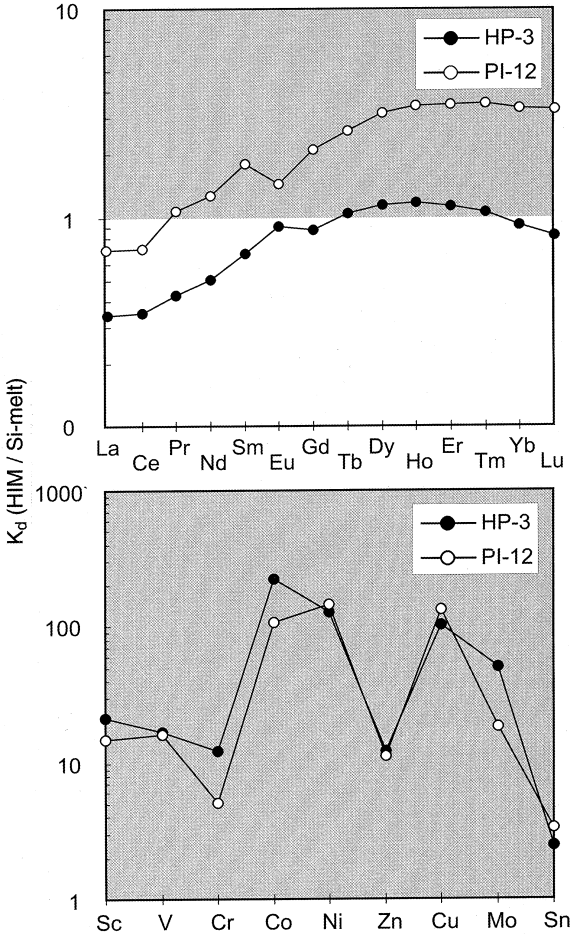

Fig. 11 Partition coefficients for REE (top) and selected transition elements and base metals (bottom) in conjugate HIM and trachyte melts

Parameters controlling HIM composition and its immiscible separation

The liquid line of descent is strongly influenced by the oxidation state of the parental magma. High f_{O_2} values result in the Bowen crystallization trend, when most iron is bound in early crystallizing magnetite, $Fe^{2+}Fe^{3+}_2O_4$, leaving residual melts enriched in silica. In contrast, low f_{O_2} (e.g., below the NNO buffer, Philpotts and Doyle 1983) and more reducing conditions result in accumulation of early cumulus spinel (Fe^{2+}, Mg)Al_2O_4. The excess iron concentrates in the residual melts, giving rise to the Fenner crystallization trend. The iron-oversaturated melts may potentially split to form silica- and iron-rich conjugate phases.

In gabbroic cumulates of the Western Carpathians, oxygen fugacity was about –1.3 log units below QFM during clinopyroxene accumulation. The earliest spinel superimposed to the cpx, was pleonaste, indicating that reducing conditions maintained during crystallization of postcumulus phases. Relatively low f_{O_2} during the latest differentiation are indicated by pronounced Eu anomalies in plagioclases and low Fe^{3+} contents in the glass pockets hosted in syenitic xenoliths. Local magnetite, coexisting with Y,Ca-silicates and Nb,Th,U-oxides, might imply less reducing conditions. Hypersthene and ilmenite – the only iron-bearing minerals of granitic xenoliths – and extremely low Fe^{3+} contents in associated rhyolitic glass again reflect reducing conditions.

Melt inclusions are microscopic equivalents of a closed magmatic system. The cpx-hosted melt inclusions in gabbroic xenolith clearly document that a trachyte liquid can be derived from alkalic trachybasalt by ~60 vol.% fractionation of kaersutite and ~5 vol. % of pleonaste. The residual melt associated with these minerals is however almost totally devoid of iron (< 0.3 wt%). This leads us to conclude that spinel and associ-

ated kaersutite accumulate enough iron to preclude generation of an iron-rich residual melt.

In contrast, silicic glasses hosted in syenitic and granitic xenoliths contain as much as 3–6 wt% of FeO. As inferred from simple mass balance recalculations in Tables 2 and 3, the initial FeO_{tot} content in the trachytic glasses must have reached 11 wt% prior to exsolution of HIM and crystallization of mafic minerals (magnetite, phlogopite). The mechanism by which such iron-enriched silicic liquids could originate remains unclear.

In the Pliocene maar near Pinciná, most of the titanium in the melt has been used up by ulvöspinel, ilmenite and Ti-rich kaersutite during early differentiation, and an additional Ti-aluminosilicate phase must have exhausted all remaining TiO_2 during later differentiation. The residual liquids have thus been Ti-depleted, giving rise to Fe-dominated HIM. In contrast to Pinciná, TiO_2-dominated HIM occurs at the Pleistocene tuff cone near Hodejov, despite the fact that the TiO_2 content in the host amphibole is similar to that from Pinciná (Table 2). This suggests either a different magmatic source and/or the HIM exsolved prior to precipitation of the Ti-bearing phases. The first possibility seems realistic, because the host amphibole is also substantially less Fe-rich and more magnesian compared to that from Pinciná.

Judging from the later onset of HIM separation in more oxidising (high Fe^{3+}) syenitic xenoliths, low f_{O_2} values seem to promote two-liquid magmatic immiscibility. This is, however, in disagreement with experimental work, which document exsolution of a magnetite-like melt in the $K(Na)AlSi_3O_8$-FeO-Fe_2O_3-SiO_2 system under strongly oxidising conditions (e.g., Naslund 1983).

Conclusions

1. Gabbroic (clinopyroxene-plagioclase, amphibole-plagioclase), syenitic and granitic xenoliths represent fragments of a differentiated alkali basalt intruding into the lower and middle crust.
2. Hydrous (10–20% H_2O) iron oxide- and titanium oxide liquids have exsolved from trachybasalt-to-rhyolite melts during fractionation of the parental alkali basalt over the temperature range of 1180–900 °C.
3. The immiscible separation results in REE fractionation between conjugate high-iron (HIM) and silicic melts.
4. Apart from HREE, the HIM strongly concentrates some additional elements, particularly transition elements and base metals. Extremely high HIM/Si-melt partition coefficients have been recorded for Co (160 ± 60), Cu (110 ± 10), Mo (34 ± 16), Sc (18 ± 4), V (15 ± 1), Zn (11.5 ± 0.5) and Cr (8.5 ± 3.5), and moderately high ones for Ta (3.3 ± 1.3), Nb (2.7 ± 1.3), Sn (2.8 ± 0.3), Sr (2.8 ± 1), and Y (2.4 ± 1). In contrast, Li (0.18 ± 0.1), Rb (0.14 ± 0.05), Cs (0.31 ± 0.03), La (0.50 ± 0.16) and Ce (0.53 ± 0.19) have always partitioned into coexisting trachyte melt.
5. Immiscible separation can effectively modify trace element characteristics of the parental melt, generating a silicic melt fraction depleted particularly in transition elements and HREE, and enriched in LREE, Li, Rb and Cs.

Acknowledgements The study was financially supported from the Alexander von Humboldt Foundation (Germany). Electron microprobe data were obtained within the framework of the Slovak Geological Survey project No. 17-517-01/07: Geodynamic development of the Western Carpathians – Interpretation of deep structure. B. Mysen generously shared his computer program for melt structure calculations. The manuscript has greatly benefited from comments of A. Philpotts, E. Roedder, and an anonymous reviewer.

References

Anders E, Grevesse N (1989) Abundances of the elements: meteoritic and solar. Geochim Cosmochim Acta 53: 197–214

Angus S, Armstrong B, De Reuck KM (1976) International thermodynamic tables of the liquid state. Carbon dioxide. Pergamon, Oxford

Armstrong JT (1988) Quantitative analysis of silicate and oxide minerals: comparison of Monte Carlo, ZAF and phi-rho-z procedures. In: Newbury DE (ed) Microbeam analysis – 1988. San Francisco Press, San Francisco

Aspen P, Upton BGJ, Dickin AP (1990) Anorthoclase, sanidine and associated megacrysts in Scottish alkali basalts: high-pressure syenitic debris from upper mantle sources ? Eur J Mineral 2: 503–517

Barrés O, Burneau A, Dubessy J, Pagel M (1987) Application of micro-FT-IR spectroscopy to individual hydrocarbon fluid inclusion analysis. Appl Spectrosc 41: 1000–1008

Blank JG, Brooker RA (1994) Experimental studies of carbon dioxide in silicate melts: solubility, speciation, and stable carbon isotope behavior. In: Carroll MR, Holloway JR (eds) Volatiles in magmas. (Reviews in Mineralogy vol. 30). Mineralogical Society of America, Washington DC, pp 157–186

Dobson PF, Epstein S, Stolper EM (1989) Hydrogen isotope fractionation between coexisting vapor and silicate glasses and melts at low pressure. Geochim Cosmochim Acta 53: 2723–2730

Ellison AJG, Hess PC (1989) Solution properties of rare earth elements in silicate melts: inferences from immiscible liquids. Geochim Cosmochim Acta 53: 1965–1974

Fine GJ, Stolper EM (1985) The speciation of carbon dioxide in sodium aluminosilicate glasses. Contrib Mineral Petrol 91: 105–121

Förster HG, Jafarzadeh A (1994) The Bafq mining district in central Iran – a highly mineralized Infracambrian volcanic field. Econ Geol 89: 1697–1721

Frietsch R (1978) On the magmatic origin of iron ores of the Kiruna type. Econ Geol 73: 478–485

Frost BR (1991) Introduction to oxygen fugacity and its petrologic importance. In: Lindsley DH (ed) Oxide minerals: petrologic and magnetic significance. (Reviews in Mineralogy vol. 25). Mineralogical Society of America, Washington DC, pp 1–9

Green TH (1994) Experimental studies of trace-element partitioning applicable to igneous petrogenesis – Sedona 16 years later. Chem Geol 117: 1–36

Grzechnik A, Zimmermann HD, Hervig RL, King PL, McMillan PF (1996) FTIR micro-reflectance measurements of the CO_3^{2-} ion content in basanite and leucitite glasses. Contrib Mineral Petrol 125: 311–318

Guo JF, Green TH, O'Reilly SY (1992) Ba partitioning and the origin of anorthoclase megacrysts in basaltic rocks. Mineral Mag 56: 101–107

Hoefs J (1997) Stable isotope geochemistry (4th edn). Springer, Berlin Heidelberg New York

Huraiová M, Konečný P, Konečný V, Simon K, Hurai V (1996) Mafic and felsic igneous xenoliths in late Tertiary alkali basalts: fluid inclusions and mineralogical evidence for a deep-crustal magmatic reservoir in the Western Carpathians. Eur J Mineral 8: 901–916

Ihinger PD, Hervig RL, McMillan PF (1994) Analytical methods for volatiles in glasses. In: Carroll MR, Holloway JR (eds) Volatiles in magmas (Reviews in Mineralogy vol. 30). Mineralogical Society of America, Washington DC, pp 67–121

Irving AJ, Frey FA (1984) Trace element abundances in megacrysts and their host basalts: constraints on partition coefficients and megacryst genesis. Geochim Cosmochim Acta 48: 1201–1221

Keppler H (1989) The influence of the fluid phase composition on the solidus temperatures in the haplogranite system $NaAlSi_3O_8$-$KAlSi_3O_8$-SiO_2-H_2O-CO_2. Contrib Mineral Petrol 102: 321–327

Konečný P, Konečný V, Lexa J, Huraiová M (1995) Mantle xenoliths in alkali basalts of Southern Slovakia. Acta Vulcanol 7: 241–247

Konečný V, Lexa J, Balogh K, Konečný P (1995) Alkali basalt volcanism in Southern Slovakia: volcanic forms and time evolution. Acta Vulcanol 7: 167–171

Le Maitre RW (1989) A classification of igneous rocks and glossary of terms. Blackwell, Oxford

Lindsley DH (1983) Pyroxene thermometry. Amer Mineral 68: 477–493

McCarthy TC, Patiño Douce AE (1997) Experimental evidence for high-temperature felsic melts formed during basaltic intrusions of the deep crust. Geology 25: 463–466

Mysen BO (1991) Relations between structure, redox equilibria of iron, and properties of magmatic liquids. In: Perchuk LL, Kushiro I (eds) Physical chemistry of magmas (Advances Phys Chem. vol. 9). Springer, Berlin Heidelberg New York, pp 41–98

Mysen BO, Virgo D (1978) Influence of pressure, temperature and bulk composition on melt structures in the system $NaAlSi_2O_6$-$NaFe^{3+}Si\ Si_2O_6$. Am J Sci 278: 1307–1322

Mysen BO, Virgo D (1985) Iron-bearing silicate melts: relations between pressure and redox equilibria. Phys Chem Minerals 12: 191–200

Mysen BO, Virgo D (1989) Redox equilibria, structure, and properties of Fe-bearing aluminosilicate melts: relationships among temperature, composition, and oxygen fugacity in the system Na_2O-Al_2O_3-SiO_2-Fe-O. Amer Mineralogist 74: 58–76

Naslund HR (1983) The effect of oxygen fugacity on liquid immiscibility in iron-bearing silicate melts. Am J Sci 283: 1034–1059

Naumov VB, Solovova IP, Kovalenker VA, Rusinov VL (1993) Immiscibility in acidic magmas: evidence from melt inclusions in quartz phenocrysts of ignimbrites. Eur J Mineral. 5: 937–941

Nimis P (1995) A clinopyroxene geobarometer for basaltic systems based on crystal-structure modelling. Contrib Mineral Petrol 121: 115–125

Nystrøm JO, Henriquez F (1994) Magmatic features of iron ores of the Kiruna type in Chile and Sweden; ore textures and magnetite geochemistry. Econ Geol 89: 820–839

Otten MT (1984) The origin of brown hornblende in the Artfjället gabbro and dolerites. Contrib Mineral Petrol 86: 189–199

Park CF Jr (1961) A magnetite "flow" in northern Chile. Econ Geol 56: 431–441

Philpotts AR (1967) Origin of certain iron-titanium oxide and apatite rocks. Econ Geol 62: 303–315

Philpotts AR (1982) Compositions of immiscible liquids in volcanic rocks. Contrib Mineral Petrol 80: 201–218

Philpotts AR, Doyle CD (1983) Effect of magma oxidation state on the extent of silicate liquid immiscibility in a tholeiitic basalt. Am J Sci 283: 967–986

Pupin JP (1980) Zircon and granite petrology. Contrib Mineral Petrol 73: 207–220

Roedder E (1979) Silicate liquid immiscibility in magmas. In: Yoder HS Jr (ed) The evolution of the igneous rocks. Fiftieth Anniversary Perspective. Princeton University Press, Princeton, pp 15–57

Roedder E, Weiblen PW (1971) Petrology of silicate melt inclusions, Apollo 11 and Apollo 12 and terrestrial equivalents. Proc 2nd Lunar Sci Conf vol. 1, pp 507–528

Ryerson FJ, Hess PC (1978) Implication of liquid-liquid distribution coefficients to mineral-liquid partitioning. Geochim Cosmochim Acta 42: 921–932

Sterner SM, Bodnar RJ (1989) Synthetic fluid inclusions – VII. Re-equilibration of fluid inclusions in quartz during laboratory-simulated metamorphic burial and uplift. J Metamorphic Geol 7: 243–260

Sterner SM, Pitzer KS (1994) An equation of state for carbon dioxide valid from zero to extreme pressures. Contrib Mineral Petrol 117: 362–374

Turner SP, Foden JD, Morrison RS (1992) Derivation of some A-type magmas by fractionation of basaltic magma: an example from the Padthaway Ridge, South Australia. Lithos 28: 151–179

Valley JW, Chiarenzelli JR, McLelland JM (1994) Oxygen isotope geochemistry of zircon. Earth Planet Sci Lett 126: 187–206

Van der Marel HW, Beutelspacher H (1976) Atlas of infrared spectroscopy of clay minerals and their admixtures. Elsevier, Amsterdam

Vicenzi EP, Green TH, Sie SH (1992) Immiscible silicate liquids at elevated pressure: the influence of melt structure on elemental partitioning. EOS Trans Am Geophys Union 74: 341

Vicenzi EP, Green TH, Sie SH (1994) Effect of oxygen fugacity on trace-element partitioning between immiscible silicate melts at atmospheric pressure: a proton and electron microprobe study. Chem Geol 117: 355–360

Vityk MO, Bodnar RJ (1995) Textural evolution of synthetic fluid inclusions in quartz during reequilibration, with applications to tectonic reconstruction. Contrib Mineral Petrol 121: 309–323

Vityk MO, Bodnar RJ, Dudok IV (1996) Fluid inclusions in "Marmarosh Diamonds": evidence for tectonic history of the Folded Carpathian Mountains, Ukraine. Tectonophysics 255: 163–174

Watson BE (1976) Two-liquid partition coefficients: experimental data and geochemical implications. Contrib Mineral Petrol 56: 119–134

Watson BE, Cherniak DJ (1997) Oxygen diffusion in zircon. Earth Planet Sci Lett 148: 527–544

Wiechert U, Hoefs J (1995) An excimer laser-based micro analytical preparation technique for in-situ oxygen isotope analysis of silicate and oxide minerals. Geochim Cosmochim Acta 59: 4093–4101